# Thin Film Nanotube Transistors Based on Self-Assembled, Aligned, Semiconducting Carbon Nanotube Arrays

**Michael Engel,[†] Joshua P. Small,[†] Mathias Steiner,[†] Marcus Freitag,[†] Alexander A. Green,[‡] Mark C. Hersam,[‡] and Phaedon Avouris[†,*]**

[†]IBM T. J. Watson Research Center, Yorktown Heights, New York 10598, and [‡]Department of Materials Science and Engineering and Department of Chemistry, Northwestern University, Evanston, Illinois, 60208

**ABSTRACT** Thin film transistors (TFTs) are now poised to revolutionize the display, sensor, and flexible electronics markets. However, there is a limited choice of channel materials compatible with low-temperature processing. This has inhibited the fabrication of high electrical performance TFTs. Single-walled carbon nanotubes (CNTs) have very high mobilities and can be solution-processed, making thin film CNT-based TFTs a natural direction for exploration. The two main challenges facing CNT-TFTs are the difficulty of placing and aligning CNTs over large areas and low on/off current ratios due to admixture of metallic nanotubes. Here, we report the self-assembly and self-alignment of CNTs from solution into micron-wide strips that form regular arrays of dense and highly aligned CNT films covering the entire chip, which is ideally suitable for device fabrication. The films are formed from pre-separated, 99% purely semiconducting CNTs and, as a result, the CNT-TFTs exhibit simultaneously high drive currents and large on/off current ratios. Moreover, they deliver strong photocurrents and are also both photo- and electroluminescent.

**KEYWORDS:** thin film · self-assembly · carbon nanotube · alignment · field-effect transistor · opto-electronic

Until recently, most TFT research has involved organics and amorphous silicon as the active channel material.[1,2] Several groups tried to take advantage of the high-performance nature of the CNT field-effect transistor and fabricate CNT-TFTs with mobilities higher than those of organic-based TFTs.[3,4] The CNT-TFTs demonstrated to date have employed films of mixed (metallic and semiconducting) CNTs in random orientation. Low-coverage CNT-TFT devices function in the percolation regime and can have $I_{on}/I_{off}$ ratios as high as $10^5$; however, they provide low levels of on-state drive current due to their large sheet resistance, $R_{\square} \sim 1.4$ MΩ/sq,[5] where $R_{\square} \equiv RW/L$, and R, W, and L are the resistance, width, and length of the device, respectively. Attempts to improve the on-state current by increasing CNT density have increased the number of metallic pathways between source and drain, and degraded the $I_{on}/I_{off}$ ratio to 1−2 orders of magnitude.[5−8] Recently, an approach was published which aimed at suppressing the contribution from metallic CNTs by functionalizing the $SiO_2$ substrate with an amine-terminated silane.[9] This approach produced low current TFT devices with very high sheet resistance $R_{\square} \sim 23$ MΩ/sq.[9] In another, more recent approach, percolation transport in randomly oriented CNTs in very long (~100 μm) channels patterned with narrow trenches was used to reduce the influence of the metallic nanotubes and produce nicely performing plastic CNT-FETs.[10] However, as the authors of this study pointed out for shorter channel TFTs, pre-enriched semiconducting CNTs will be needed.[10]

We have resolved this problem by fabricating CNT-TFTs directly from high purity, semiconducting (~99%) CNTs produced by density gradient ultracentrifugation.[11] We quantitatively evaluated the degree of separation in the sample solution on the single-tube device level (see the Methods section), while other studies have so far provided only qualitative estimates.[9] Our CNT films exhibit 1−2 orders of magnitude higher normalized average conductance, corresponding to a sheet resistance of $R_{\square} \sim 200$ kΩ/sq, while maintaining high $I_{on}/I_{off}$ ratios ($10^3-10^4$ in the case of our $L_c = 4$ μm devices). To controllably deposit aligned nanotube films in a superlattice-like structure on the insulating substrate, we combine two different principles. First, it is known that long nanotubes in solution tend to adopt a nematic liquid crystal alignment.[12] This is easily explained by their cylindrical structure which favors a lateral

*Address correspondence to avouris@us.ibm.com.

Received for review October 23, 2008 and accepted November 23, 2008.

**Published online December 9, 2008.**
10.1021/nn800708w CCC: $40.75

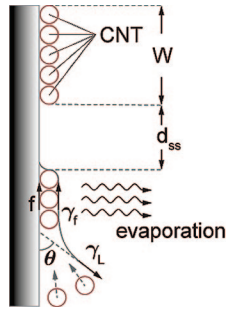


**Figure 1. Cross-sectional schematic illustrating the slip-stick mechanism responsible for self-assembly of the superlattice of single-walled carbon nanotubes (CNT).**

alignment as explained as early as 1949 by Onsager on the basis of his excluded volume entropy model.[13] This tendency is favored even further if one includes the anisotropy of the attractive intermolecular interactions among nanotubes, which also favor parallel alignment as in the Maier−Saupe mean field theories.[14−16] To transfer this nanotube alignment to the solid and, moreover, to produce the superlattice, we employ a long-known, empirical observation commonly known as "the coffee ring phenomenon". This involves the ring-like residue observed when a droplet of coffee (or other insoluble material) is allowed to evaporate on a surface. A detailed explanation of the physics of the phenomenon did not appear until relatively recently,[17−20] and since then, the details of the phenomenon have been studied in a number of solvent−solute systems and substrates. It was found that not only a single ring but also concentric rings can be formed under appropriate conditions.[21,22] Here we only give a simple qualitative picture of the process and refer the reader to the literature for a detailed analysis.

When a planar substrate is immersed vertically in the nanotube solution, a thin meniscus is formed at the solid−liquid−vapor interface (contact line). As the solvent evaporates, convective transport brings the aligned nanotubes in the liquid to the contact line and they deposit on the substrate. The surface roughness thus generated produces a frictional force, *f*, which together with the liquid surface tension, $\gamma_f$, pins the position of the contact line (Figure 1).[34] As evaporation proceeds, the capillary force, $\gamma_L$, which pulls the liquid inward, builds up and eventually the contact line becomes depinned. The contact line then jumps to a new position where it is subsequently pinned again by the deposition of a new row, and so on. The resulting stick-slip motion of the liquid forms the superlattice of CNT strips (Figure 2). The spacing between successive rows of CNTs depends on the pinning probability, which in turn depends, among other factors, on the concentration of the solution. High concentration implies easy pinning, so the slip part of the motion is short, the contact gets easily repinned, leading to closely spaced nanotube rows.

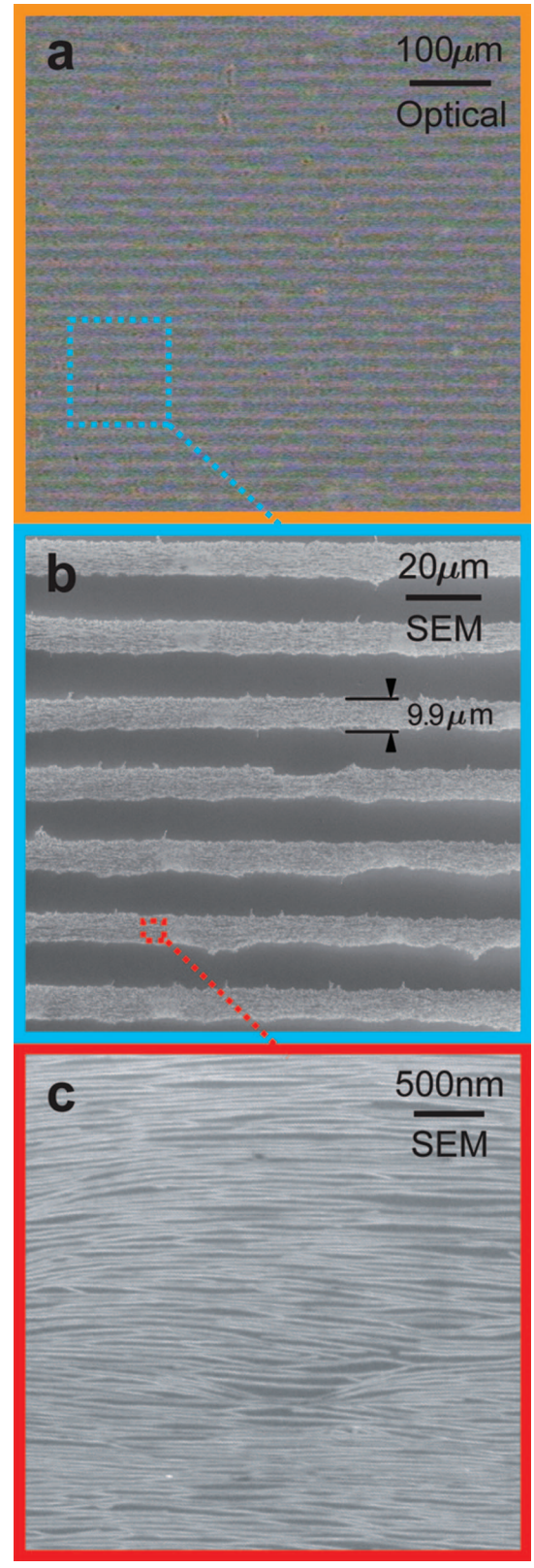


**Figure 2. (a) Optical micrograph showing the large scale alignment of the nanotube superlattice. Dashed lines highlight positions of the stripes. (b) SEM micrograph of the nanotube superlattice. (c) SEM micrograph of nanotubes within a strip.**

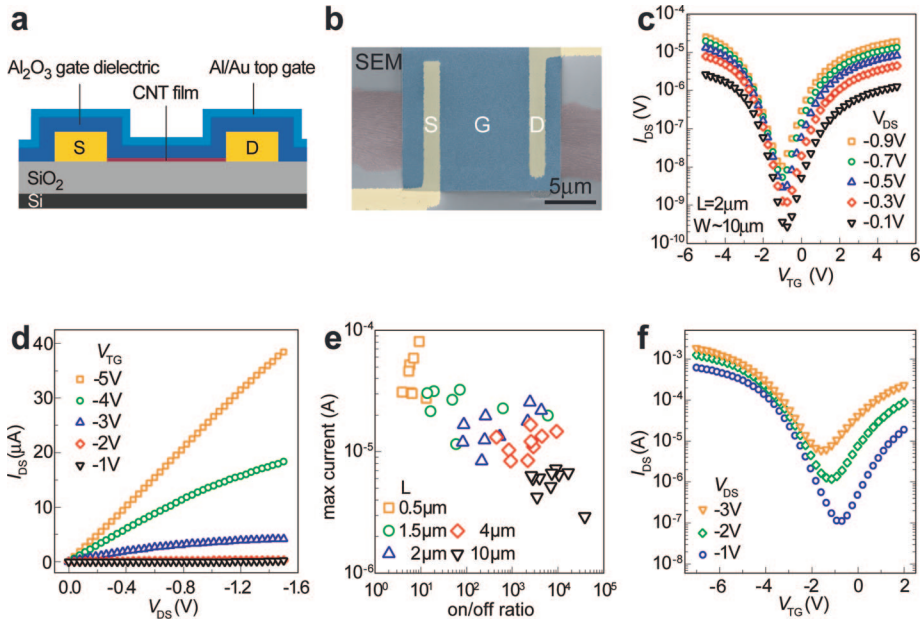


**Figure 3. (a) CNT-TFT device schematic. (b) SEM micrograph of a typical device. (c,d) Electrical characteristics for a typical CNT-TFT device. (e) On-state current plotted against on/off ratio for all devices in the study. As the device length increases, the maximum current slowly drops, while strongly increasing the on/off ratio. (f) *I versus* $V_g$ of a device having nine strips in parallel.**

## RESULTS AND DISCUSSION

Experimentally, in order to produce a regular array of CNTs such as that shown in Figure 2a,b, we partially submerged a $Si/SiO_2$ substrate in a glass vial containing nanotubes. We used 99% purity semiconducting arc-discharge CNTs suspended in 1% SDS aqueous solution, with a diameter range $1.3 < d < 1.7$ nm, as confirmed by micro-Raman spectroscopy studies (see Figure S1 in Supporting Information). We vibrationally isolated the setup by placing it on an optical table and protected the setup further by placing it under a bell jar. After solvent evaporation, we observe large regions (extending 6 mm down the length of an 8 mm wide sample) of regularly spaced horizontal "strips" of nanotubes (Figure 2a). Both the width of the strips and the strip spacing in Figure 2b are about 10 μm. This method of self-assembly yields a much higher degree of nanotube self-alignment than that generated by nanomaterial spin-coating: virtually all nanotubes lie within 5° of one another, as compared with spin-coating methods, yielding 71% of tubes lying within 20° of one another.[9] Moreover, the superlattice structure produced by this evaporation-driven self-assembly technique has not been achieved by other nanotube alignment methods. The nanotube film height was measured by AFM, yielding values ranging from 1 to 6 nm and indicating that the film composition is a mixture of individual and bundled CNTs. The micron-scale lateral dimensions and nanometer size film heights that we measure are consistent with the scale of patterns seen in other slip-stick-driven deposition phenomena.[23−25]

The strips of oriented CNTs were subsequently used to fabricate CNT-TFT devices of varying source-drain separation ($d_{sd}$ = {0.5, 1, 2, 4, 10 μm}). Panels a and b of Figure 3 show the device schematic and SEM image of a typical CNT-TFT device, respectively. Details of the fabrication process can be found in the Methods section. We note that the metallic layers of the gate-stack are purposefully thin ($t = 8$ nm), with a transmittance of $T > 50\%$ in the infrared, allowing us to probe the CNT-TFT devices through the top gate by optical means. In total, we fabricated 10−20 devices at each source-drain length, in addition to a number of high-current devices where we contacted multiple CNT strips in parallel.

Electrical characteristics of a typical device ($L_c = 2$ μm) are shown in Figure 3c,d. We observe ambipolar $I-V$ behavior[4] with the current minimum located at a

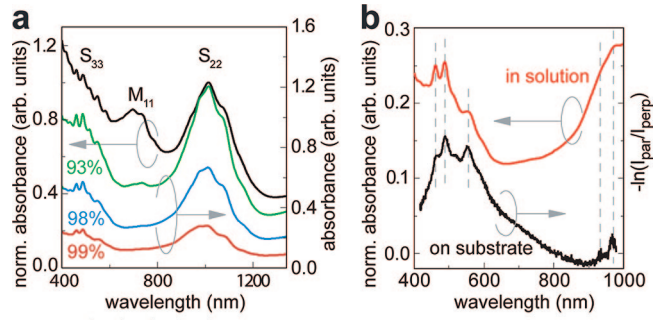


**Figure 4. (a) Visible/near-infrared absorption data from purified semiconducting nanotube solutions. The unsorted starting material (black curve) exhibits a distinct $M_{11}$ metallic peak, as compared with the 99% purely semiconducting CNT solution (red) used in this study. (b) On-substrate absorption data (black curve) after CNT strip formation without the absorption background from the solution. The on-substrate film data show a pronounced semiconducting $S_{33}$ peak and no measurable contribution from $M_{11}$.**

gate bias of $V_g \sim -1$ V. In the particular case of the $L_c = 2$ μm, $W = 10$ μm device, whose characteristics are shown in Figure 3c,d, we find an $I_{on}/I_{off}$ ratio of $10^4$ and an on-state conductance of ~25 μS. The corresponding drift mobility of this device is $\mu \approx 10$ cm$^2$/V · s.

To disentangle the effects of metallic nanotubes from those of nanotube−nanotube interactions and percolation processes, we fabricated CNT-TFTs with channel lengths ranging from $L_c = 0.5L_s$ to $10L_s$, where the average length of the CNTs is $L_s \sim 1$ μm. We first discuss the short channel devices where $L_c \leq 1.5$ μm. Figure 3e plots $I_{on}$ *versus* $I_{on}/I_{off}$ for all devices measured in our study. The shortest channel $L_c = 500$ nm devices display high on-state conductances of $G_{on} \sim 50$ μS, but suffer from weak switching, reflected in the $I_{on}/I_{off}$ ratio which is less than 10. To estimate the metallic content of the purified material, we measured the absorption spectrum of the solution and of the deposited film. Figure 4a shows absorption spectra of different fractions of the density gradient centrifuged material. Our samples are made from material where essentially no metallic $M_{11}$ absorption band is visible (99% pure). Following assembly of the films on the substrate, we measured the absorption spectrum in Figure 4b (black curve). It also shows the $S_{22}$ and $S_{33}$ semiconducting transitions without any contribution from the $M_{11}$ band. In order to detect the possible presence of a small fraction of metallic tubes not detected in the optical measurements, we measured the electrical characteristics of a large number of individual, single CNT devices fabricated from semiconducting nanotube enriched material. Of the 83 single-tube devices we fabricated, 82 were found to be semiconducting with only 1 metallic CNT (Figure S2 in Supporting Information). However, a simple model of 99% semiconducting and 1% metallic CNTs bridging the source and drain contacts in parallel would naively predict an $I_{on}/I_{off} \sim 10^2$, which is inconsistent with our findings.

While the starting material is heavily enriched with semiconducting CNTs, the existence of different CNT species along with variations of the local environment within the film leads to variation of the threshold voltage, $V_T$, among the individual CNTs composing the CNT-TFT. From our electrical characterization of short channel CNT-TFTs, we observe a spread in values of $V_T$ which roughly matches the width of the off-state in these ambipolar film devices. Because the measured output characteristics of the CNT-TFTs are ensemble-averaged over numerous individual tubes, the minimum off-state current is raised from that of a single tube device leading to the low $I_{on}/I_{off}$ ratio.

While the average length of our tubes is $L_s \sim 1$ μm, there is a distribution about this length, so that slightly longer tubes have a nonzero probability of bridging the contacts of the $L_c = 1.5$ μm devices. Around this critical length scale, $L_c \sim L_s$, where the transport mechanism changes from direct transport to percolation, device characteristics are expected to vary widely. Indeed, in the case of $L_c = 1.5$ μm devices, we find the largest distribution of $I_{on}/I_{off}$ ratios, ranging from $10^1$ to $10^4$.

We now turn to a discussion of transport in the $L_c > L_s$ regime, which has attracted a great deal of interest lately, both theoretically[26−30] and experimentally.[5−8,10,33] In this regime, the source and drain are not directly connected by individual CNTs, and so the charge transport is governed by percolation. There have been a number of numerical studies of percolation-driven transport in randomly oriented 2D networks of CNTs, exploring the variation of conductivity as a function of the length, CNT density, intertube coupling, and degree of film alignment.[26−30] The first requirement for percolation controlled transport is that the device tube density, ρ, must exceed some critical tube density, $\rho_c$, so that the randomly positioned tubes can form an uninterrupted electrical path between the source and drain. In random 2D rigid rod films, this critical density has been found to be $\rho \sim 1/\langle L_s \rangle^2$. The conductance obeys a power law, $G \sim L_c^{-n}$, and for tube densities just above the critical density, the scaling exponent falls in the range $1 < n < 2$. As the CNT density in the film increases past the critical density for onset of percolation conduction, $n$ approaches 1. Log−log plots of $G_{on}$ *versus* $L_c$ for our devices reveal a critical scaling exponent of $n = 0.7$. The deviation from $n = 1$ is caused by the non-ohmic contact resistance, $R_c$, between the tubes and the metal electrodes arising from the existence of Schottky barriers. Studies in partially aligned films determined that near the percolation threshold the conductance exhibits a power law dependence on the alignment angle, $G \sim \theta^{-\kappa}$.[29,30] Despite the strong degree of CNT alignment, our film densities ($\rho \sim 10-20/\mu m^2$) are high enough that we are always far beyond the critical density needed for percolation transport.

Aside from studies employing electrical breakdown[31] to remove metallic from semiconducting tubes,[32,33] until now, percolation-driven CNT-TFTs have always utilized as-prepared CNTs containing typically a 2:1 ratio of semiconducting to metallic CNTs.[5−8,10] By adjusting the density of the CNT films as a means to control percolation, a necessary tradeoff is made between the $I_{on}/I_{off}$ ratio and the on-state conductance, $G_{on}$. Electrical studies of high density films report low values of the sheet resistance ($R_\square \sim 400\ \Omega$/sq − 20 kΩ/sq) but make no mention of $I_{on}/I_{off}$.[8] Other CNT-TFT studies also measure fairly low values of $R_\square \sim 35$ k − 580 kΩ/sq;[5] however, the $I_{on}/I_{off}$ ratio was less than 10. Lowering the nanotube density succeeded in raising $I_{on}/I_{off}$ to $10^5$, but the sheet resistance increased to $R_\square \sim 1.5$ MΩ/sq.[5] Medium density CNT-TFTs have also been reported, lying in the middle of the two extremes, with $R_\square \sim 265$ kΩ/sq and $I_{on}/I_{off} \sim 70$.[6]

In order to escape the above-discussed tradeoff between high on-state conductance and switching abil-

ity, it is therefore necessary to make CNT-TFTs from purified semiconducting CNTs. Indeed, Figure 3e shows that by using 99% semiconducting CNT-TFTs we are able to substantially increase $I_{on}/I_{off}$ without negatively affecting our on-state conductance. Specifically, the $L_c = 4$ μm devices exhibit an average sheet resistance of $R_\square = 200$ k ± 50 kΩ/sq, with $I_{on}/I_{off}$ falling in the range of 400−9000. Increasing the channel length to $L_c = 10$ μm, we find the average sheet resistance to be $R_\square \sim 168$ k ± 62 kΩ/sq, and $I_{on}/I_{off} \sim 2500-40\,000$. These values are well suited for TFT operation.

The carrier drift mobility was calculated using the standard formula $\mu = (L_c t_{ox}/\epsilon_{eff} V_{sd} W)(dI/dV_g)$, where $t_{ox}$ is the oxide thickness and $\epsilon_{eff}$ is the effective dielectric constant of the oxide material. We make the approximation $\epsilon_{eff} = (\epsilon_{SiO_2} + \epsilon_{Al_2O_3})/2$ to account for the inhomogeneous dielectric environment, where $\epsilon_{SiO_2} = 3.9\epsilon_0$ and $\epsilon_{Al_2O_3} = 6.7\epsilon_0$ (for $T = 90$ °C deposited $Al_2O_3$) yielding $\epsilon_{eff} = 5.3\epsilon_0$. Calculations of mobility in our CNT-TFT devices give values in the range of $\mu \sim 5-20$ cm$^2$/V·s, much higher than the typical mobilities of organic TFTs, but significantly lower than those of single CNT-FETs ($\mu \sim 1-2 \times 10^3$ cm$^2$/V·s). One obvious reason for this disparity is the high tube−tube coupling resistance in the films.[28] This coupling resistance between nanotubes is quoted to be as high as 100 MΩ,[8] which clearly dominates the nanotube resistance (~10 kΩ) and reduces the overall device mobility.

In addition to the coupling resistance, we propose here an additional, more fundamental reason for the difference in the on-state performance between individual CNT devices and a CNT-TFT which involves the mutual screening interactions between CNTs. Theoretical studies of CNT-TFT performance as a function of CNT spacing have demonstrated that the on-state characteristics of CNT-TFTs degrade rapidly with decreasing CNT separation, leading to a lowering of the on-state current and device mobility.[35] While the density of CNTs along the width of our device is 10−20/μm, the CNT distribution is not completely uniform. Due to limits in AFM and SEM lateral resolution, it is difficult to distinguish individual and bundled nanotubes in images; however, AFM measurements of film height indicate that some degree of bundling is very likely. Bundling of nanotubes would imply that the nanotube−nanotube spacing is much less than the thickness of the 15 nm gate oxide, which controls screening by the metal gate, allowing the CNTs to screen one another and thus reduce the effectiveness of the gate in switching the device.

One obvious strategy for reducing the effects due to tube−tube and tube−contact interactions is to reduce the amount of bundling among CNTs. This may be possible by adjusting the nature and amount of surfactant present in the CNT solution, and studies are performed along those lines. An alternative method for minimizing intertube interaction is to decrease the length scale over which the CNT−CNT screening interaction becomes important. In fact, this length scale should depend exponentially on the gate insulator dielectric constant.[35] In our case, changing the top gate oxide from $Al_2O_3$ to a high-*k* dielectric material such as $HfO_2$ should have a strong impact on the performance of such CNT-TFT devices.

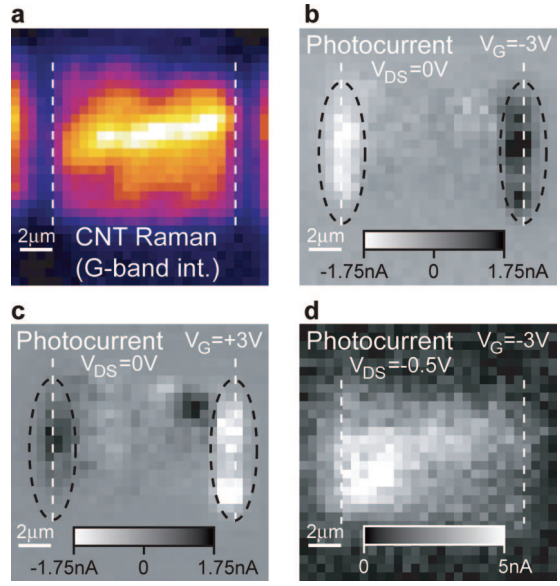


**Figure 5. (a) Raman (G-phonon) image of a CNT strip. The inner edges of source and drain electrodes are indicated by vertical white dashed lines. (b,c) Short-circuit photocurrent images showing local, opposite polarity maxima at the Schottky barriers formed at the CNT−electrode interfaces (highlighted by dashed ellipses), as well as local potential drops in the active channel. (d) AC photocurrent image indicating a smooth potential drop (on the scale of the optical resolution, 0.5 μm) and exhibiting a current maximum which spatially coincides with the topography maximum as measured by the AFM.**

Further insight into the origin of the CNT film resistance is provided by optical measurements. Figure 5a shows a Raman G-phonon band intensity map of a $L_c = 10$ μm CNT-TFT, imaged through its top gate. The Raman intensity correlates well with the local nanotube density as measured by AFM (data not shown) and gives an image of the spatial distribution of CNTs. In Figure 5b−d, we use photocurrent microscopy to image built-in electric fields and potential drops in the TFT.[36] The technique uses a focused laser to locally produce electron−hole pairs in the CNTs. The generated photocurrent is proportional to the local electric field that separates the electron and hole. This field can be due to Schottky barriers, defects, other internal fields, or an external bias. At zero bias, the main features in the photocurrent images are the Schottky barriers, which are distributed along the entire width of the nanotube film and switch sign by going from p-type to n-type conduction (see areas surrounded by dotted lines in Figure 5b,c). We also observe an occasional film defect (dark spot) such as the one in Figure 5c on the

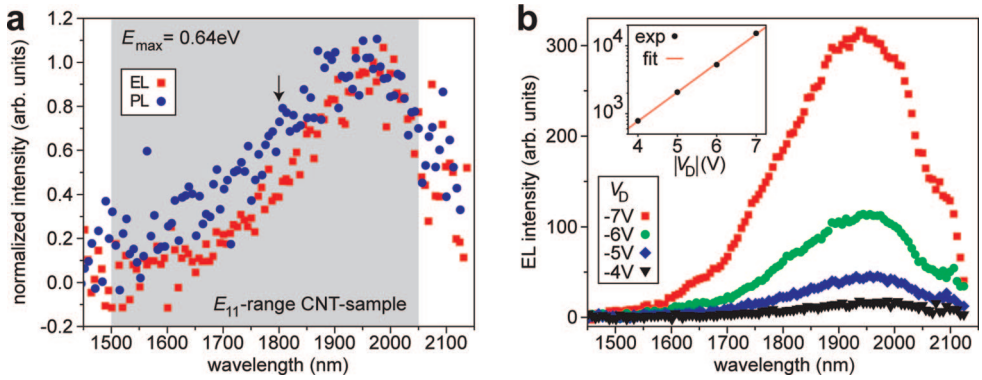


**Figure 6. Infrared emission from CNT-TFTs. (a) Comparison of photoluminescence (PL) and electroluminescence (EL) spectra acquired from an $L_c$ = 1 μm CNT-TFT. PL was laser-excited at λ = 514.5 nm, in resonance with CNTs that emit around 1800 nm (indicated by arrow). EL was excited at $V_D$ = −4 V. The shaded area indicates the range of emission wavelengths ($\lambda_{11}$ values) of nanotubes that are present in the TFT. (b) Electroluminescence spectra at different drain voltages. Inset: semilog plot of the integrated EL intensity.**

right. On the other hand, by applying a small bias of −0.5 V in the p-type on-state, the entire interior of the TFT shows some contrast due to the potential steps at the numerous tube−tube contacts (Figure 5d). This behavior is not observed in single CNT devices,[37] but it is consistent with a percolating current through TFTs.

Due to the efficiency of semiconducting-to-metallic nanotube excited state energy transfer, dense, unseparated CNT films do not luminesce. This quenching inhibits the use of CNT films in opto-electronic applications. To investigate the behavior of our films, we have measured the emission from a CNT-TFT, excited with a laser (photoluminescence) and electrically (electroluminescence) (Figure 6a).[36] The photoluminescence (PL) was excited at λ = 514.5 nm, in resonance with the $E_{33}$ transitions of nanotubes whose emission peak is expected to be around $\lambda_{11}$ = 1800 nm (indicated by an arrow). Instead of observing an emission peak in this spectral region, however, we measure a red-shifted spectrum with a broad peak around 1940 nm. The electroluminescence (EL) spectrum, excited at a drain voltage of −4 V, has a slightly narrower spectrum, which also peaks at 1940 nm. The low-energy onsets of both PL and EL overlap and coincide with the $E_{11}$ transitions of the largest diameter nanotubes present in the film (diameter $d$ ∼ 1.7 nm). For comparison, we have shaded the region of $\lambda_{11}$ values that corresponds to the entire diameter distribution present in the CNT film.

Increasing the drain voltage leads to an exponential increase in electroluminescence intensity (Figure 6b).[36,38] The low-energy EL onset, however, is not affected by the drain voltage, and the fwhm increases only slightly from 240 to 280 nm when going from $V_d$ = −4 to −7 V. Even at highest voltages, the spectral width stays well below the width that would correspond to the entire diameter distribution of the CNTs in the film (from 1500 to 2050 nm). Two effects play a role in reducing the observed spectral width and moving the emission maximum toward longer wavelengths: (1) The current is carried predominantly by the larger diameter tubes because they exhibit smaller Schottky barriers (*i.e.*, contact resistance);[39] and (2) excitons created on the smaller diameter (higher band gap) tubes can decay into excitons on larger diameter tubes nearby.[40,41] The fwhm of the FL spectrum (350 ± 50 nm) is slightly broader than the EL spectra, which we attribute to the more efficient optical excitation of smaller diameter tubes as compared to electrical excitation. There are only few metallic tubes present in our films, so in spite of bundling, excitons on large tubes have long lifetimes, can decay radiatively, and allow opto-electronic applications.

In addition to the single-stripe devices fabricated for length-dependent electrical studies, we also fabricated devices contacting many CNT stripes in parallel. Figure 3f shows the electrical characteristics for a $W$ = 200 μm, $L_c$ = 4 μm device which contacts 10 CNT stripes in parallel. The on-state performance is very good, delivering high drive currents, $I_{on}$ > 1 mA at $V_{sd}$ = 2 V, while maintaining $I_{on}/I_{off}$ ∼ $10^3$. Such CNT-TFT devices would be very competitive with organic TFTs for electronic applications on flexible and transparent substrates.

In conclusion, by using an evaporation self-assembly method, we show that it is possible to drive alignment of CNTs on both the macro- and microscale. This unique alignment method facilitates the fabrication of highly dense and aligned CNT-TFTs, ideal for electronic applications. The large, aligned active device area will be useful for applications such as sensors or opto-electronics. Furthermore, by using 99% enriched semiconducing CNTs as a basis for our CNT-TFTs, we overcome a fundamental problem of tradeoff between $G_{on}$ and $I_{on}/I_{off}$ associated with CNT-TFTs which employ as-grown metallic/semiconducting CNT mixtures.

## METHODS

**Sample Fabrication.** After the CNT self-assembly process, we rinsed the sample in ethanol, followed by rapid thermal annealing for $t = 60$ s at $T = 600$ °C in Ar. We patterned sparse arrays of alignment marks onto the striped CNT region using e-beam lithography (EBL) followed by metal deposition (Ti/Au) and liftoff. A second EBL step defined source and drain electrodes on the CNT stripes. Next we evaporated Ti = 1 nm/Pd = 40 nm/Au = 20 nm as contact metals and performed another liftoff process. We then opened windows in the PMMA resist around each device by EBL, followed by atomic layer deposition (ALD) of a 15 nm $Al_2O_3$ film at 90 °C, and then 15 nm of evaporated Al film. The ALD deposition was performed at 90 °C to prevent degradation of the PMMA. This Al/$Al_2O_3$ mask protected the devices during a subsequent oxygen plasma etching step to remove extraneous CNTs and electrically isolate the devices from one another. The etch mask was removed by wet-etching in $H_3PO_4$. Finally, a fourth EBL step defined the region for a top gate, where the gate stack is composed of 15 nm of ALD deposited $Al_2O_3$ and Al = 2 nm/Au = 6 nm.

**Single Nanotube Device Study.** A low density nanotube solution (from the same purified source used to make the CNT-TFTs) was spun coat onto a $Si/SiO_2$ substrate. Source and drain electrodes (with 400 nm spacing) were patterned onto the nanotubes at random using EBL followed by metal deposition (Ti/Pd/Au). SEM imaging revealed 83 devices with exactly one CNT bridging the source and drain electrodes. Subsequent *I versus* $V_g$ measurements of these 83 single-tube devices (Figure S2 in Supporting Information) show that 82 CNTs are semiconducting and only 1 is metallic, providing solid evidence of semiconducting CNT enrichment. In conjunction with the visible/near-infrared absorption data, we are confident in stating 99% semiconducting enrichment of our nanotube starting material.

**Optical Absorption Measurements.** Optical absorption measurements of the as-deposited CNT films were done in reflection using a microscope objective (100×, NA = 0.8, Nikon). White light from a Xe lamp was focused onto individual CNT stripes, and the reflected light was sent into a spectrometer (Triax 322, Jobin Yvon/Horiba) equipped with a grating having a groove density of 150 $mm^{-1}$ and a $LN_2$-cooled charge coupled device (Spectrum One, Jobin Yvon/Horiba) as detector. Reference spectra were taken at bare substrate positions between the CNT stripes and used to normalize the measured intensities. The reflection spectra are dominated by the effect of the CNT film thickness on the reflection properties of the silicon/silicon oxide substrate. To obtain a measure of the absorption of individual CNT stripes, we make use of the highly aligned nature of the CNTs in the stripe and their strong polarization anisotropy, by dividing two of these spectra taken with 90° rotated polarization.

**Photo- and Electroluminescence Measurements.** Photo- (PL) and electroluminescence (EL) spectra were detected with a liquid-nitrogen-cooled HgCdTe detector. A transmission grating fabricated on top of a prism was used as a wavelength dispersive element. The spectra are corrected for both the low-pass (cold) filter transmission and the spectrally varying efficiency of the grating.

**Micro-Raman Measurements.** Raman images and spectra were acquired using a scanning optical microscope equipped with a standard microscope objective (100×, NA = 0.8, Nikon) providing a focal spot diameter of about 0.5 μm. A feedback-controlled piezoelectric scanning stage (P-527.2CL, PI) accomplished raster scanning of the CNT device with respect to the microscope objective with nanometer precision. As excitation light source, we used an $Ar^+$ laser (Innova 300, Coherent) operated 514.5 nm. The laser light was tightly focused onto individual CNT stripes (*i.e.*, through the optically transparent top gate in the device configuration), and the Raman-scattered light was separated from the laser excitation light using a suitable holographic notch filter (Kaiser) and spectrally analyzed using a spectrograph (Triax 322, Jobin Yvon/Horiba) equipped with a grating having a groove density of 1200 $mm^{-1}$ and a $LN_2$-cooled charge coupled device (Spectrum One, Jobin Yvon/Horiba) as detector. The resulting spectral resolution was 8 $cm^{-1}$ (fwhm).

*Acknowledgment.* We thank G. Tulevski for technical advice and useful discussions, and Bruce Ek for his expert technical assistance. A.A.G. and M.C.H. acknowledge support from the National Science Foundation (DMR-0520513, EEC-0647560, and DMR-0706067).

*Supporting Information Available:* RBM spectrum of CNT stripe, micro-Raman images of the same section of CNT stripe taken at two different RBM frequencies, and *I versus* $V_g$ measurements of 83 single tube CNT devices. This material is available free of charge *via* the Internet at http://pubs.acs.org.

## REFERENCES AND NOTES

1. Dimitrakopoulos, C. D.; Mascaro, D. J. Organic Thin-Film Transistors: A Review of Recent Advances. *IBM J. Res. Dev.* **2001**, *45*, 11–27.
2. Forrest, S. R. The Path to Ubiquitous and Low-Cost Organic Electronic Appliances on Plastic. *Nature* **2004**, *428*, 911–918.
3. *Carbon Nanotubes: Advanced Topics in the Synthesis, Structure, Properties and Applications*; Jorio, A., Dresselhaus, M., Dresselhaus, G., Eds.; Springer: New York, 2008.
4. Avouris, Ph.; Chen, Z.; Perebeinos, V. Carbon Based Electronics. *Nat. Nanotechnol.* **2007**, *2*, 605–615.
5. Snow, E. S.; Novak, J. P.; Campbell, P. M.; Park, D. Random Networks of Carbon Nanotubes as an Electronic Material. *Appl. Phys. Lett.* **2003**, *82*, 2145–2147.
6. Snow, E. S.; Campbell, P. M.; Ancona, M. G.; Novak, J. P. High-Mobility Carbon Nanotube Thin-Film Transistors on a Polymeric Substrate. *Appl. Phys. Lett.* **2005**, *86*, 033105-1–033105-3.
7. Artukovic, E.; Kaempgen, M.; Hecht, D. S.; Roth, S.; Gruner, G. Transparent and Flexible Carbon Nanotube Transistors. *Nano Lett.* **2005**, *5*, 757–760.
8. Hu, L.; Hecht, D. S.; Gruner, G. Percolation in Transparent and Conducting Carbon Nanotube Networks. *Nano Lett.* **2004**, *4*, 2513–2517.
9. LeMieux, M. C.; Roberts, M.; Barman, S.; Jin, Y. W.; Kim, J. M.; Bao, Z. Self-Sorted, Aligned-Nanotube Networks for Thin-Film Transistors. *Science* **2008**, *321*, 101–104.
10. Cao, Q.; Kim, H. S.; Pimparkar, N.; Kulkarni, J. P.; Wang, C.; Shim, M.; Roy, K.; Alam, M. A.; Rogers, J. A. Medium-Scale Carbon Nanotube Thin-Film Integrated Circuits on Flexible Plastic Substrates. *Nature* **2008**, *454*, 495–500.
11. Arnold, M. S.; Green, A. A.; Hulvat, J. F.; Stupp, S. I.; Hersam, M. C. Sorting Carbon Nanotubes by Electronic Structure Using Density Differentiation. *Nat. Nanotechnol.* **2006**, *1*, 60–65.
12. Song, W.; Kinloch, I. A.; Windle, A. H. Nematic Liquid Crystallinity of Multiwall Carbon Nanotubes. *Science* **2003**, *302*, 1363.
13. Onsager, L. The Effects of Shape on the Interaction of Colloidal Particles. *Ann. N.Y. Acad. Sci.* **1949**, *51*, 627–659.
14. Maier, W.; Saupe, A. Eine Einfache Molekulare Theorie des Nematischen Kristallinflüssigen Zustandes. *Z. Naturforsch.* **1959**, *13a*, 564–566.
15. Maier, W.; Saupe, A. Eine Einfache Molekular-Statistische Theorie der Nematischen Kristallinflüssigen Phase Teil 1. *Z. Naturforsch.* **1959**, *14a*, 882–889.
16. Maier, W.; Saupe, A. Eine Einfache Molekular-Statistische Theorie der Nematischen Kristallinflüssigen Phase Teil 2. *Z. Naturforsch.* **1960**, *15a*, 287–292.
17. Deegan, R. D.; Bakajin, O.; Dupont, T. F.; Huber, G.; Nagel, S. R.; Witten, T. A. Capillary Flow as the Cause of Ring Stains from Dried Liquid Drops. *Nature* **1997**, *289*, 827–829.
18. Fischer, B. J. Particle Convection in an Evaporating Colloidal Droplet. *Langmuir* **2002**, *18*, 60–67.
19. Deggan, R. D.; Bakajin, O.; Dupont, T. F.; Huber, G.; Nagel, S. R.; Witten, T. A. Contact Line Deposits in an Evaporating Drop. *Phys. Rev. E* **2000**, *62*, 756–765.
20. Popov, Y. O. Evaporative Deposition Patterns: Spatial Dimensions of the Deposit. *Phys. Rev. E* **2005**, *71*, 036313-1–036313-17.

21. Adachi, E.; Dimitrov, A. S.; Nagayama, K. Stripe Patterns Formed on a Glass Surface During Droplet Evaporation. *Langmuir* **1995**, *11*, 1057–1060.
22. Shmuylovich, L.; Shen, A. Q.; Stone, A. Surface Morphology of Drying Latex Films: Multiple Ring Formation. *Langmuir* **2002**, *18*, 3441–3445.
23. Xu, J.; Xia, J.; Hong, S. W.; Lin, Z.; Qui, F.; Yang, Y. Self-Assembly of Gradient Concentric Rings *via* Solvent Evaporation from a Capillary Bridge. *Phys. Rev. Lett.* **2006**, *96*, 066104-1–066104-4.
24. Lin, Z.; Granick, S. Patterns Formed by Droplet Evaporation from a Restricted Geometry. *J. Am. Chem. Soc.* **2005**, *127*, 2816–2817.
25. Xu, J.; Xia, J.; Lin, Z. Evaporation-Induced Self-Assembly of Nanoparticles from a Sphere-on-Flat Geometry. *Angew. Chem., Int. Ed.* **2007**, *46*, 1860–1863.
26. Kumar, S.; Murthy, J. Y.; Alam, M. A. Percolating Conduction in Finite Nanotube Networks. *Phys. Rev. Lett.* **2005**, *95*, 066802-1–066802-4.
27. Alam, M. A.; Pimparkar, N.; Kumar, S.; Murthy, J. Theory of Nanocomposite Network Transistors for Macroelectronics Applications. *MRS Bull.* **2006**, *31*, 466–470.
28. Kumar, S.; Pimparkar, N.; Murthy, J. Y.; Alam, M. A. Theory of Transfer Characteristics of Nanotube Network Transistors. *Appl. Phys. Lett.* **2006**, *88*, 123505-1–123505-3.
29. Pimparkar, N.; Kocabas, C.; Kang, S. J.; Rogers, J.; Alam, M. A. Limits of Performance Gain of Aligned CNT Over Randomized Network: Theoretical Predictions and Experimental Validation. *IEEE EDL* **2007**, *28*, 593–595.
30. Behnam, A.; Ural, A. Computational Study of Geometry-Dependent Resistivity Scaling in Single-Walled Carbon Nanotube Films. *Phys. Rev. B* **2007**, *75*, 125432.
31. Collins, P.; Arnold, M.; Avouris, Ph. Engineering Carbon Nanotubes and Nanotube Circuits Using Electrical Breakdown. *Science* **2001**, *292*, 706–709.
32. Kang, S. J.; Kocabas, C.; Ozel, T.; Shim, M.; Pimparkar, N.; Alam, M. A.; Rotkin, S. V.; Rogers, J. A. High-Performance Electronics Using Dense, Perfectly Aligned Arrays of Single-Walled Carbon Nanotubes. *Nat. Nanotechnol.* **2007**, *2*, 230–236.
33. Zhou, Y.; Gaur, A.; Hur, S. H.; Kocabas, C.; Meitl, M. A.; Shim, M.; Rogers, J. A. p-Channel, n-Channel Thin Film Transistors and p-n Diodes based on Single Wall Carbon Nanotube Networks. *Nano Lett.* **2004**, *4*, 2031–2035.
34. de Gennes, P. G. Wetting: Statics and Dynamics. *Rev. Mod. Phys.* **1985**, *57*, 827–863.
35. Leonard, F. Crosstalk Between Nanotube Devices: Contact and Channel Effects. *Nanotechnology* **2006**, *17*, 2381–2385.
36. Avouris, Ph.; Freitag, M.; Perebeinos, V. Carbon-Nanotube Photonics and Optoelectronics. *Nat. Photonics* **2008**, *2*, 341–350.
37. Lee, E. J. H.; Balasubramanian, K.; Dorfmueller, J.; Vogelgesang, R.; Fu, N.; Mews, A.; Burghard, M.; Kern, K. Electronic Band Structure Mapping of Nanotube Transistors by Scanning Photocurrent Microscopy. arXiv:0705.3407v1, arxiv.org e-Print archive; http://lanl.arxiv.org/abs/0705.3407v1, 2007.
38. Perebeinos, V.; Avouris, Ph. Impact Excitation by Hot Carriers in Carbon Nanotubes. *Phys. Rev. B* **2006**, *74*, 121410-1–121410-4.
39. Adam, E.; Aguirre, C. M.; Marty, L.; St-Antoine, B. C.; Meunier, F.; Desjardins, P.; Menard, D.; Martel, R. Electroluminescence from Single-Wall Carbon Nanotube Network Transistors. *Nano Lett.* **2008**, *8*, 2351–2355.
40. Qian, H.; Georgi, C.; Anderson, N.; Green, A. A.; Hersam, M. C.; Novotny, L.; Hartschuh, A. Exciton Energy Transfer in Pairs of Single-Walled Carbon Nanotubes. *Nano Lett.* **2008**, *8*, 1363–1367.
41. Tan, P. H.; Rozhin, A. G.; Hasan, T.; Hu, P.; Scardaci, V.; Milne, W. I.; Ferrari, A. C. Photoluminescence Spectroscopy of Carbon Nanotube Bundles: Evidence for Exciton Energy Transfer. *Phys. Rev. Lett.* **2007**, *99*, 137402-1–137402-4.